Research Square

Preprints are preliminary reports that have not undergone peer review.
They should not be considered conclusive, used to inform clinical practice,
or referenced by the media as validated information.

# A three-stage metabolic switch links root-zone water status to phloem fiber growth and defense in Salix suchowensis

**Hongbing Zheng**

zhenghb@ahau.edu.cn

Anhui Agricultural University

**Research Article**

**Keywords:** Salix suchowensis, groundwater table depth, phloem fiber, secondary cell wall, metabolomics

**Posted Date:** November 24th, 2026

**DOI:** https://doi.org/10.21203/rs.3.rs-11505076/v1

**License:** This work is licensed under a Creative Commons Attribution 4.0 International License.
Read Full License

**Additional Declarations:** No competing interests reported.

# A three-stage metabolic switch links root-zone water status to phloem fiber growth and defense in *Salix suchowensis*

Hongbing Zheng[a,*]

a. Anhui Agricultural University, Hefei 230036, P. R. China.

**Correspondence:** Hongbing Zheng

**ORCID:** 0009-0007-1395-2819

**Email:** zhenghb@ahau.edu.cn

**Address:** No. 130, Changjiang West Road, Shushan District, Hefei City, Anhui Province, P. R. China.

**Funding:** This work was supported by the Major Project of the Chinese Academy of Engineering–Local Cooperation (2024-DFZD-64).

**Abstract:** How woody plants adjust bark-fiber development to groundwater-table gradients—and the underlying root-zone soil moisture regimes—is central to understanding riparian tree acclimation and the developmental regulation of bark secondary walls. Eight- to ten-year-old *Salix suchowensis* plants were compared at groundwater table depths of 1.2 (CK), 0.6 (T1), 0.5 (T2), 0.4 (T3) and 0.3 m (T4), integrating fiber morphology, growth traits, and cell-wall cellulose, hemicellulose and lignin with widely targeted metabolomics and weighted gene co-expression network analysis (WGCNA). Fiber development followed a threshold-type, three-stage response. The deep-water control set the baseline (wall-to-lumen ratio, RR, 0.65); the adequate-water state (T1/T2) defined a wall-construction window, with fiber length peaking at T1 and RR falling to 0.52–0.56; the shallow-water state (T3/T4) shifted development toward wall thickening and defense, with RR reaching 0.92 at T4. Wall components peaked in strict succession: cellulose at T1 (418 mg g−1, +18.8%) before falling 38.8% by T4; lignin transiently at T3 (199 mg g−1, +68.7%); and hemicellulose latest at T4 (464 mg g−1, +39.8%). Carbon was redirected from glycolysis and the pentose phosphate pathway through the shikimate–phenylpropanoid network toward flavonoids, tannins, salicinoids and hemicellulose. WGCNA independently identified a cellulose-associated module (ME5, r = +0.94) and a hemicellulose-associated module (ME9, r = −0.89). The ordered carbon-sink succession from cellulose to lignin and then to hemicellulose and terminal defense adds metabolite-level timing to the growth–differentiation balance framework and reveals root-zone water status as a physiological switch governing bark development between structural growth and chemical defense.

**Keywords:** *Salix suchowensis*; groundwater table depth; phloem fiber; secondary cell wall; metabolomics

## 1 Introduction

*Salix suchowensis* W.C.Cheng (Salicaceae) is a riparian shrub endemic to China, mainly distributed along the Yellow River, the Huai River, and the middle and lower reaches of the Yangtze River. It exhibits strong environmental adaptability, tolerance to both drought and flooding, and a well-developed root system, making it an excellent species for slope and embankment stabilization. Its long, flexible annual shoots are underpinned by well-developed bark phloem fibers with specialized secondary walls, providing a useful woody system in which to examine how secondary-wall development and bark defense respond to a fluctuating water regime (Baker et al., 2022). The groundwater table determines root-zone moisture and oxygen conditions: when the water table is too deep, root water uptake is restricted and the plants tend toward drought; when the water table is too shallow, the root zone becomes hypoxic and waterlogged (Kreuzwieser & Rennenberg, 2014; Mozo et al., 2021). Previous studies on Salix have focused mainly on whole-plant physiology, and preliminary drought-metabolic analyses have been reported for S. suchowensis (Jia et al., 2020). However, two questions remain unanswered: How does the groundwater table alter the fiber wall structure of the bark (periderm and secondary phloem)? And which changes in carbon flux through metabolic pathways support this structural alteration?

The bark (periderm and secondary phloem), which performs photosynthate transport, mechanical support and defense, sits at a critical interface of the crown–stem–root continuum and reflects the plant's adaptive strategy to environmental change. The morphological characteristics of bark phloem fibers are typically described by fiber length (FL), fiber width (FW), lumen diameter (LD), double-wall thickness (DWT), and the ratios of length-to-width (SR), lumen-to-width (LR), and wall-to-lumen (RR). Anatomically, slender, large-lumen, thin-walled fibers predominate during elongation, whereas increased DWT and RR mark secondary-wall thickening and a shift toward mechanical support. Cellulose forms the microfibril skeleton, hemicellulose the matrix, and lignin the hydrophobic reinforcement; their ratios directly determine these morphological traits (Oktaee et al., 2017). To date, the genetics and expression regulation of height and wood formation have been investigated in S. suchowensis

(Chen et al., 2024; Wei et al., 2022). However, how phloem fibers and the three major wall components vary with groundwater table fluctuations, and which differential metabolites correspond to these variations, remain to be systematically elucidated.

Metabolomics can simultaneously detect pathway products such as sugars, organic acids, amino acids, phenylpropanoids, and flavonoids, making it suitable for tracking carbon flux direction (Obata & Fernie, 2012). *S. suchowensis* has been genome-sequenced and upgraded to a chromosome-level assembly, providing a foundation for integrating metabolomics and phenotypes (Dai et al., 2014; Wei et al., 2020). Metabolome–transcriptome integration studies on willow bark have also been reported (Zhou et al., 2022). Nevertheless, the metabolic switches driving these structural transitions remain unclear: at which water status fibers shift from elongation to wall thickening, how the three wall components rise and fall in order along this transition, and which phenylpropanoid nodes dominate the reallocation of carbon from wall construction to chemical defense.

## 2 Materials and Methods

### *2.1 Experimental materials and design*

The experiment was conducted in November 2025 along the Gu River in Funan County, Anhui Province, China (115.8037°E, 32.6317°N). The experimental materials were ten-year-old Salix suchowensis W.C.Cheng plants established from cuttings in a plantation. Based on a preliminary field survey, five groundwater table depth treatments were established: CK (1.2 m, deep water table), T1 (0.6 m), T2 (0.5 m), T3 (0.4 m), and T4 (0.3 m, shallow water table); shallower depths corresponded to higher root-zone soil water content. By root-zone water status, these regimes are referred to hereafter as the deep-water (CK), adequate-water (T1/T2), and shallow-water (T3/T4) states. Each treatment comprised four replicated plots (2 m × 2 m). Within each plot, uniform annual shoots were selected and measured (20, 26, 13, 18 and 18 valid shoots for CK–T4, respectively; Table S1). Bark peeled from the basal stem of the selected shoots was pooled per plot into one composite sample, one portion oven-dried at 60 °C for fiber maceration and wall-component assays and the other flash-frozen in liquid nitrogen (−80 °C) for metabolomic analysis. For metabolomics, three composite samples per treatment were analyzed (15 in total); the four plot composites per treatment were used for the cell-wall assays (n = 4). At sampling, plant height and basal, middle, and tip diameters were recorded as four growth traits. These four traits, together with seven fiber morphological traits and the three wall-component traits, formed the 14 phenotypes used in the joint and network analyses. Their descriptive statistics, raw shoot-level values, and integrated treatment means are presented in Tables S1 and S2.

The study site lies on the alluvial plain of the Gu River in the Huang-Huai Plain, at an elevation of 20–30 m a.s.l. The region has a warm temperate monsoon climate, with a mean annual temperature of 15.4 °C, hot and rainy summers and dry winters, and most rainfall concentrated in summer. The plantation occupies a natural micro-topographic gradient on the riverbank, along which the groundwater table becomes progressively shallower towards the river. To characterize this gradient, fifteen groundwater observation wells were installed across the site, and the plots of the five treatments were arranged parallel to the wells along the depth gradient, corresponding

to groundwater table depths of 1.2 (CK), 0.6 (T1), 0.5 (T2), 0.4 (T3) and 0.3 m (T4) measured at the respective positions and confirmed at sampling.

The experimental plants were ten-year-old Salix suchowensis W.C.Cheng propagated from cuttings and planted at a spacing of 0.3 m (between rows) × 0.4 m (within rows). The plantation is managed under the traditional local coppice system, in which the annual shoots are harvested once a year by flat cutting at the stump, leaving the root stump to re-sprout; all shoots measured in this study were therefore one-year-old annual shoots regenerated from the stumps during the current growing season. No irrigation or fertilization was applied during the experiment, so plant growth depended entirely on the natural groundwater regime. Before measurement, plant height and ground diameter were surveyed along the gradient and only uniform, healthy plants were selected.

### *2.2 Determination of bark fiber morphology*

Bark was cut into thin strips and macerated with acetic acid–hydrogen peroxide (1:1) at 60 °C for 4–8 h until the fibers dispersed completely (Franklin, 1945). After safranin staining, slides were imaged under a Motic BA-210D light microscope. FL, FW, LD and DWT (the sum of the two secondary-wall thicknesses) were measured with Image-Pro Plus, and SR (FL/FW), LR (LD/FW) and RR (DWT/LD) were calculated. Approximately 90 intact fibers were measured per treatment (22–23 per plot; Table S3).

### *2.3 Determination of the contents of three major cell-wall components in phloem fibers*

Cellulose, hemicellulose and lignin were determined with assay kits (Beijing Solarbio Science & Technology Co., Ltd., Beijing, China) by UV-visible spectrophotometry: cellulose as glucose after acid hydrolysis (anthrone–sulfuric acid method, 620 nm), hemicellulose as reducing sugars (3,5-dinitrosalicylic acid method, 540 nm), and lignin by the acetyl bromide method (280 nm). Contents were calculated from kit standard curves as mg g−1 dry weight. Four biological replicates per treatment were each assayed in triplicate (technical replicates averaged; statistical analyses used biological replicates, n = 4; Table S4); percentage changes were calculated from unrounded means.

### *2.4 Widely targeted metabolomic analysis*

Samples were freeze-dried (Scientz-100F) and ground, and 50 mg was extracted with 1,200 μL of −20 °C pre-cooled 70% methanol containing internal standards; after vortexing, the mixture was centrifuged (4 °C, 12,000 rpm) and the supernatant filtered (0.22 μm). Widely targeted detection was performed by ultra-performance liquid chromatography–electrospray ionization tandem mass spectrometry (UPLC-ESI-MS/MS) (Chen et al., 2013) using an ExionLC™ AD system (SCIEX) equipped with an Agilent SB-C18 column (1.8 μm, 2.1 mm × 100 mm). Gradient elution was carried out with water containing 0.1% formic acid (A) and acetonitrile (B) at a flow rate of 0.35 mL min−1, a column temperature of 40°C, and an injection volume of 2 μL. Data were acquired in multiple reaction monitoring (MRM) mode on an ESI triple quadrupole. Identification was performed against the MetWare self-built plant widely targeted database (MWDB). Data were acquired with Analyst 1.6.3 and integrated with MultiQuant, and relative quantification was based on MRM peak areas. Three pooled quality-control (QC) samples (QC01–QC03, equal aliquots of all samples) monitored instrumental stability throughout the batch. For each metabolite, any missing value was imputed as 20% of the smallest peak area recorded for that compound across the dataset, and metabolites whose QC coefficient of variation exceeded 0.5 were removed before downstream analysis. A total of 1,351 metabolites were detected.

For mass spectrometric acquisition, the UPLC system was coupled to an electrospray ionization triple quadrupole–linear ion trap (QTRAP) mass spectrometer (SCIEX) operating in MRM mode. The ESI source temperature was 500 °C, the ion spray voltage was +5,500 V in positive ion mode and −4,500 V in negative ion mode, ion source gases I and II and the curtain gas were set at 50, 60 and 25 psi, respectively, and the collision-activated dissociation parameter was set to high. The linear gradient elution program was: 0.00 min, 5% B; 9.00 min, 95% B (held for 1 min); 10.00–11.10 min, linear decrease to 5% B; and re-equilibration at 5% B until 14.00 min. For each metabolite, one quantifier and one qualifier MRM transition were monitored, with pairwise-optimized declustering potentials and collision energies scheduled by retention-time window. The 70% methanol extraction solvent contained an internal

standard (working concentration 250 μg $mL^{-1}$ from a 1,000 μg $mL^{-1}$ stock). Peak annotation followed the widely targeted workflow of Chen et al. (2013): a feature was assigned when its retention time and precursor–product ion pair (Q1/Q3) matched the MetWare self-built plant widely targeted database (MWDB, plant widely targeted metabolome database V1.0). A full table of all 1,351 annotated peaks (Table S12) reports each metabolite's name, chemical class, Q1 and Q3 m/z values, ion mode, molecular formula, CAS and KEGG identifiers; retention time, declustering potential, collision energy and the identification basis (validation by authentic standards or matching against the in-house standard spectral library and retention time) are additionally provided for 30 representative metabolites spanning the pathways analysed.

***2.5 Screening and functional annotation of differentially accumulated metabolites***

Peak areas were log2-transformed and unit variance (UV)-scaled. A PCA of all 1,351 metabolites (QC excluded) was first performed for an unbiased overview (Fig. 3A), followed by orthogonal partial least squares discriminant analysis (OPLS-DA (Trygg & Wold, 2002); MetaboAnalystR) with one predictive and one orthogonal component and seven-fold cross-validation ($Q^2$(cum) > 0.5 indicating a valid model). Robustness against over-fitting was assessed by 200 response permutations (Table S11). Differentially accumulated metabolites (DAMs) were screened using variable importance in projection (VIP) ≥ 1.0 and |log2FC| ≥ 1 (FC ≥ 2 or ≤ 0.5). A total of 419 DAMs were identified, and t-test p values and Benjamini–Hochberg-adjusted false discovery rates (FDRs) were reported. Functional annotation was based on KEGG pathways and MWDB Class I chemical classification. Using the 381 detected metabolites with KEGG annotations as the background, a one-sided hypergeometric test was performed with Benjamini-Hochberg correction (Benjamini & Hochberg, 1995). The Rich factor was used to represent the degree of enrichment, and only pathways with ≥2 hits were included (Table S5). In addition, enrichment factors of up- and down-regulated DAMs in each comparison were calculated by chemical class, and bubble plots were used to show their enrichment and depletion directions during stage transitions (Fig. 6A). DAM tables, cluster assignments and raw peak areas are presented in Tables S6–S8.

### *2.6 Data analysis methods*

Statistical analyses were performed in R 4.5.0 and SPSS Statistics 26. Replicated plots were the experimental unit (n = 4); individual fibers were treated as subsamples nested within plots (plot means used for testing), and biological replicates as the unit for metabolomics (n = 3). Differences among treatments were tested by one-way ANOVA followed by Tukey's HSD test ($p < 0.05$); Pearson correlation was used for approximately normal variables and Spearman otherwise. Linear and quadratic regressions were fitted to treatment means (n = 5) to describe non-linearity and were not used for inference. Metabolite–phenotype correlations (n = 5) were treated as exploratory; only entries with $|r| \geq 0.85$, $p < 0.05$ and directions independently supported by pathway position and WGCNA were interpreted. A PCA of Z-score-standardized fiber-morphology traits provided an integrated morphological overview (Fig. 1C). K-means clustering (K = 8, selected from between-cluster variance gain and the silhouette coefficient (Rousseeuw, 1987)) was performed on row-standardized log10 treatment means. For weighted gene co-expression network analysis (WGCNA), modules were built at a soft-thresholding power $\beta = 8$ (scale-free fit $R^2 > 0.8$), a dynamic tree cut height of 0.78 and a minimum module size of 10; 170 unassigned DAMs formed the grey module. Treatment-mean module eigengenes were correlated with the 14 treatment-mean phenotypes (n = 5, $p < 0.05$). Correlation matrices and robust pairs are presented in Tables S9 and S10.

## 3 Results

### *3.1 Three-stage responses of fiber morphology to the groundwater table gradient*

All seven fiber morphological traits differed significantly among treatments ($p < 0.05$), but they did not increase or decrease linearly with groundwater table depth; instead, they exhibited a clear three-stage pattern (Fig. 1A). State I (CK) served as the reference baseline (FL ≈ 1,284 μm; RR = 0.65). After entering State II (T1/T2), FL and the length-to-width ratio (SR) reached their maximum values across the entire gradient at T1 (FL ≈ 1,437 μm), whereas FW, LD and LR peaked at T2 (FW 16.8 μm; LD ≈ 11.3 μm), with DWT thinnest in this period. Meanwhile, RR decreased to 0.56 (T1) and 0.52 (T2), the lowest and most similar values on the gradient, indicating that lumen expansion proceeded faster than wall thickening and that fibers were the widest, longest, and most uniform during this stage. In State III (T3/T4), FL, LD, and SR decreased, whereas DWT increased continuously from T2 and reached its maximum at T4. RR first rose to 0.67 at T3, approaching the CK level, and then sharply increased to 0.92 at T4, which was 1.41-fold and 1.77-fold that of CK and T2, respectively, ranking highest across the entire gradient. PCA (Fig. 1C) showed that the first two principal components cumulatively explained 81.1% of the variance, with CK, T1/T2 and T3/T4 separating sequentially along PC1 and converging with the global metabolomic pattern (Fig. 3A) to support the same three-stage model (Table S3).

### *3.2 Non-linear coordination between growth traits and fiber morphology*

The relationship between growth traits and fiber morphology was not a simple linear coordination but showed pronounced non-linear patterns, with the extrema of different fiber traits located at opposite ends of the plant-height sequence (Fig. 2A). The linear correlation between plant height and fiber length (FL) was −0.932 ($p = 0.021$), and a convex-up quadratic fit described this decline still better ($R^2 = 0.967$ versus 0.869 for the linear model): FL was greatest in the shortest, adequate-water plants (T1) and fell to a minimum near a height of 1.75 m among the tall shallow-water plants, . In contrast, plant height and double-wall thickness (DWT) followed a U-shaped relationship (quadratic $R^2 = 0.931$), with the thinnest walls near 1.28 m in the adequate-water plants and the thickest walls in the tallest shallow-water plants (T4). The

relationship between basal diameter and lumen diameter (LD) was likewise better described by a quadratic fit ($R^2 = 0.937$). The correlation heatmap (Fig. 2B; Pearson or Spearman as appropriate) further showed plant height negatively correlated with FL, SR and LR but positively with DWT and RR ($p < 0.05$ for FL and DWT). Hierarchical clustering (Fig. 2C) divided the treatments into T3/T4 and CK/T1/T2 branches and classified the seven fiber traits into FL/FW/LD/LR (length-lumen) and DWT/RR (wall-thickness) groups, which changed in opposite directions, corresponding to the growth state at T1/T2 and the wall-thickening state at T3/T4 (Tables S1 and S2).

### *3.3 Global metabolomic architecture supports the three-stage model*

The overall variation pattern of the metabolome was consistent with the phenotypic pattern and likewise supported the three-stage model. In the PCA (Fig. 3A), treatments separated mainly along PC1 (45.09% of variance; deep-water control most negative, adequate-water treatments most positive, shallow-water treatments near zero), and PC2 (17.36%) further resolved the adequate-to-shallow-water transition. This non-monotonic arrangement indicates a threshold-like metabolic reconfiguration rather than a linear response to the water-table gradient. Hierarchical clustering (Fig. 3B) merged T3/T4 first, then T2, T1 and CK, consistent with the three-stage division CK/(T1/T2)/(T3/T4). Among the 1,351 detected metabolites, flavonoids (338, 25.02%) and phenolic acids (222, 16.43%) were the two most abundant classes (Fig. 3C; counts of up- and down-regulated metabolites in each comparison are presented in Tables S6 and S7). Venn and UpSet analyses (Fig. 3D) showed that 1,258 metabolites (93.12%) were detected in all five treatments; and 93 were detected in fewer than four treatments, with only six confined to a single treatment. The five treatments therefore shared a highly conserved metabolic core (>93%), indicating that treatment differences arose primarily from quantitative changes in metabolite abundance rather than from qualitative gains or losses. KEGG pathway enrichment (Table S5) showed a two-tier pattern: no pathway was significant for the overall 419 DAMs after FDR correction, whereas α-linolenic acid metabolism (T3 vs CK, FDR = 0.025) and flavonoid/flavonol biosynthesis (T4 vs CK, FDR = 0.020) were significant in specific comparisons, coinciding with jasmonate precursor mobilization in early State III and flavonoid

defense convergence at T4, respectively. All OPLS-DA models fitted well ($Q^2$(cum) = 0.895–0.967; Table S11) and passed 200 response permutations (no permuted model exceeded the true model), confirming genuine rather than over-fitted separation and providing a reliable basis for the subsequent VIP screening.

### *3.4 Stage-wise clustering and stage specificity of differentially accumulated metabolites*

To characterize the trajectories of DAMs along the groundwater table gradient, K-means clustering (K = 8; Fig. 4A) was performed on row-standardized log10 means of the five treatments. Because the five treatments were sampled concurrently along a gradient rather than as a time series, the clusters and State I–III designations are interpreted as a space-for-time stage sequence rather than within-plant temporal dynamics. The 419 DAMs were grouped into four major stage-wise patterns—CK baseline, T1 peak, T3 peak, and T4 peak—together with one cluster showing a distinct double-peak pattern. The CK baseline type comprised Clusters 1/2/3 (166 metabolites in total), which were highest in CK and generally decreased as the groundwater table became shallower, and were dominated by flavonoids, organic acids, and phenolic acids; Cluster 6 (29 metabolites) showed a distinct CK/T2 double peak dominated by lipids. The T1 peak type comprised Clusters 4/5 (135 metabolites), which were lowest in CK, rose rapidly at T1 and were dominated by flavonoids, phenolic acids, amino acid derivatives and alkaloids, corresponding to early skeleton establishment in State II. The T3 peak type comprised Cluster 7 (57 metabolites, including 32 flavonoids), marking the initiation of State III and declining by T4. Cluster 8 (32 metabolites, including 11 phenolic acids, 8 flavonoids, lipids and alkaloids) rose continuously from its T1 minimum to T4, representing the convergence of multiple defense classes at the latest stage.

The stage-wise compositional differences relative to the deep-water control further revealed the succession of defense metabolism. On the up-regulated side, T1 vs CK and T2 vs CK had 110 and 94 DAMs, respectively, dominated by flavonoids and phenolic acids, indicating broad activation of the phenylpropanoid–flavonoid pathway after entering the adequate-water state (Fig. 4B). On the down-regulated side, each

comparison had 133 DAMs, and the shared down-regulated set (92) far exceeded the shared up-regulated set and was concentrated in flavonoids (37), organic acids (11) and lipids (9): CK-baseline flavonoids and some primary and membrane-lipid metabolites were thus consistently suppressed during the State I→II transition. On the up-regulated side of the shallow-water comparisons (Fig. 4C), T3 vs CK and T4 vs CK had 58 and 72 DAMs; the shared set was dominated by flavonoids (18) and phenolic acids (11), while T4-specific DAMs added terpenoids (5 vs 0 for T3), indicating an expansion from relatively simple flavonoids to a multi-class defense convergence of flavonoids, phenolic acids, alkaloids and terpenoids. On the down-regulated side, the two comparisons had 82 and 109 DAMs (union 143), exceeding the up-regulated counts and concentrated in flavonoids, organic acids and lipids: the shallow water table thus induced terminal defense accumulation while suppressing parts of primary and membrane-lipid metabolism, corroborated by the continuous withdrawal of upstream precursors in Fig. 7. Among adjacent statuses, T2 vs T1, T3 vs T2 and T4 vs T3 yielded 68, 96 and 91 DAMs; the adequate-to-shallow-water transition (T3 vs T2) was the most drastic, and T4 vs T3 was dominated by down-regulation (58/91), suggesting that reprogramming peaked in early shallow water and concluded with suppression of primary metabolism. Class enrichment across transitions (Fig. 6A) showed the same succession: flavonoid–phenolic acid shifts dominated the adequate-water transitions, whereas terpenoids, alkaloids, lignans and tannins were enriched and amino acids, lipids and organic acids depleted upon entering shallow water. Cluster assignments and DAM lists are presented in Tables S6 and S7.

### *3.5 WGCNA module–phenotype network and dynamics of the three major cell-wall components*

WGCNA assigned 249 of the 419 DAMs to 10 co-expression modules (ME1–ME10, Fig. 5A); the remaining 170 unassigned DAMs formed the grey module and were excluded from eigengene–trait correlation. Among the 10 co-expressed modules, two showed the most prominent associations with phenotypes. ME5, the largest module (103 metabolites), correlated most strongly and positively with cellulose ($r = +0.94$, $p < 0.05$) and therefore marks cellulose-based wall construction during the T1/T2 state.

ME9 (12 metabolites) was significantly and negatively correlated with hemicellulose ($r = -0.89$, $p < 0.05$), its eigengene being lowest when hemicellulose peaked late at T3/T4. At $n = 5$ these were the only two module–trait pairs reaching $p < 0.05$; all others were interpreted as trends. The accumulation trajectories of the three major wall components were clearly staggered (Fig. 5B): cellulose increased from 352 mg g−1 in CK to 418 mg g−1 in T1 (+18.8%) and then continuously decreased to only 256 mg g−1 in T4, a 38.8% decrease relative to the T1 peak; lignin increased from 118 mg g−1 to 199 mg g−1 in T3 (+68.7%), then fell to 124 mg g−1 in T4 (37.7% lower than T3, returning to near the CK level), with its peak occurring one treatment later than that of cellulose; hemicellulose showed a W-shaped pattern, increasing from 332 mg g−1 to a small peak of 421 mg g−1 at T1, decreasing to a trough of 300 mg g−1 at T2, and finally rising to 464 mg g−1 at T4 (+39.8%), reaching its peak latest. This formed an ordered succession: cellulose-dominated T1, a transient lignin rise at T3, and hemicellulose recovery at T3 with the latest peak at T4. The strictly staggered timing of the three component peaks is interpreted at the pathway level in Section 4 (raw values in Table S4; full metabolite-by-phenotype and eigengene–phenotype matrices in Table S10 and Fig. 5A).

### *3.6 Metabolic pathway reprogramming and a regulatory model linking carbon allocation to fiber development and defense*

Aligning key metabolites with fiber morphology and the three wall components by peak time yielded a metabolic–phenotypic cascade spanning the three stages (Figs. 6, 7). State I (CK) was dominated by basic primary metabolism, with relatively thin walls and no obvious secondary-wall thickening. In State II (T1/T2), vanillic acid methyl ester and γ-Glu-Trp correlated positively with cellulose ($r = +0.948$ and $+0.969$, $p < 0.05$) and cellulose peaked at T1 (418 mg g−1, +18.8% vs CK), indicating that carbon–nitrogen provisioning at the aromatic amino acid entry preferentially served wall construction. Cyanidin-3-O-glucoside, negatively correlated with DWT ($r = -0.949$), peaked at T2 during rapid lumen expansion and declined as DWT increased; FL and FW maxima also fell in this stage. In State III (T3/T4), carbon shifted to wall thickening and defense: AMP, positively correlated with lignin ($r = +0.948$), peaked at T3 alongside the lignin peak (199 mg g−1, +68.7%); the polymethoxyflavone nobiletin (r

= −0.951 with cellulose) was enriched at T4, when cellulose had fallen from 418 to 256 mg g−1 (−38.8%); the hydrolyzable tannin 1,6-di-O-galloyl-β-D-glucose correlated positively with DWT (r = +0.965) and was enriched at T4 (z = 1.50); and hemicellulose peaked latest (464 mg g−1, +39.8%) as RR rose to 0.92. The *Salix*-characteristic phenolic glycosides salicin (z = 1.71) and Helecin (z = 1.39) were also enriched at T4, constituting the *Salicaceae*-specific defense under the shallowest water table. These core metabolites, spanning the aromatic amino acid entry to the terminal flavonoid/tannin branch, depict the switch of carbon flux from wall construction to defense sinks (Table S9).

## 4 Discussion

### *4.1 Threshold-type, three-stage response of fiber morphology and growth*

Fiber morphology did not vary linearly with groundwater table depth (i.e., root-zone soil water content) but followed a threshold-type, three-stage response across the states defined in Section 2.1. As water supply improved from the deep-water baseline (RR = 0.65) to the adequate-water state, fiber length, width and lumen diameter increased together while RR fell to its gradient minimum (0.52–0.56): photosynthate was directed mainly to lumen expansion and fiber widening rather than secondary-wall deposition, rebalancing hydraulic efficiency against mechanical safety (Bryukhanova & Fonti, 2013). After the transition to shallow water, length and lumen diameter declined while double-wall thickness and RR rose, reaching 0.92 at T4 (1.77-fold the adequate-water value). This late, abrupt rise indicates that secondary-wall thickening is a discrete event triggered as the root zone moves from moist toward saturated conditions, rather than a smooth process. Once the root zone is saturated and hypoxic, trees curtail energy-costly elongation and reprogram central carbon metabolism (Daniel & Hartman, 2024; Gui et al., 2024; Kreuzwieser & Rennenberg, 2014; Quiñones Martorello et al., 2023), consistent with the growth–differentiation balance premise that growth and structural or chemical differentiation compete for the same resources (Herms & Mattson, 1992).

The growth–fiber relationship was likewise non-linear: plant height and FL were strongly negatively related (linear $r = -0.932$; quadratic $R^2 = 0.967$), the longest fibers occurring on the shortest adequate-water shoots and the shortest near a height of 1.75 m, whereas plant height and DWT followed a U-shaped relationship ($R^2 = 0.931$), with the thinnest walls near 1.28 m and the thickest on the tallest shallow-water shoots. The slender, thin-walled fibers of the elongation phase and the thick, load-bearing walls of the thickening phase thus characterized opposite ends of the height–moisture sequence rather than coinciding at a single optimum, consistent with the growth–differentiation balance hypothesis (Herms & Mattson, 1992). Because bark fibers bear mostly axial forces, plant height captures the mechanical and carbon-supply constraints on wall development, and the adequate-water construction window and the shallow-water

thickening window, rather than any single height value, anchor the metabolic interpretation that follows.

### *4.2 Central carbon–nitrogen reprogramming and the phenylpropanoid allocation switch*

To connect these morphological transitions to pathways, 89 of the 419 DAMs that could be assigned unambiguously to central carbon metabolism, the shikimate–aromatic amino acid pathway, phenylpropanoid metabolism, and cell-wall biosynthesis were selected and mapped in Fig. 7. The quality and thickening windows coincided with a coordinated reconfiguration of the central carbon–nitrogen network rather than with scattered metabolite changes (Obata & Fernie, 2012). The hexose phosphate pool was highest in the deep-water state; glycolytic intermediates (3-PGA, PEP) peaked in the early adequate-water state; and erythrose-4-phosphate, the pentose-phosphate-derived substrate that condenses with PEP at the entry of the shikimate pathway, peaked only in the late adequate-water state. This progressive shift from sugar phosphates to glycolytic intermediates to erythrose-4-phosphate indicates that glycolysis was activated first, after which carbon entered the shikimate pathway. Free pentose phosphates and pentitols of the oxidative pentose phosphate pathway were highest in the deep-water state and were drawn down continuously thereafter, but xylan and arabinoxylan—polymerized from UDP-Xyl/Ara into the backbone and side chains of hemicellulose—peaked last, in the late shallow-water state. Precursor depletion and delayed end-product deposition thus moved in opposite directions: pentose carbon was being committed to secondary wall construction, not blocked from it (Dominguez & Niittylä, 2022).

As the common gateway through which carbon enters phenylpropanoid and nitrogen-containing secondary metabolism, the shikimate pathway sets the upper limit on downstream aromatic metabolism (Maeda & Dudareva, 2012; Tzin & Galili, 2010). Aromatic amino acids and their γ-glutamyl dipeptides (for example γ-Glu-Trp) were enriched in the adequate-water state and correlated positively with cellulose, indicating accelerated aromatic carbon turnover in support of wall construction; such dipeptides also aid nitrogen reserve mobilization and reactive oxygen detoxification (Agarwal et

al., 2025; Yobi et al., 2013). At the signaling level, jasmonic acid and its isoleucine conjugate were highest in the deep-water state, methyl jasmonate peaked in the late adequate-water state, and terminal defense compounds accumulated only thereafter in shallow water—a signal-first, product-later order matching the cascade of induced defense (Kuniak & Gajewska, 2024; Li et al., 2022; Lim et al., 2017). The high basal jasmonic acid in the deep-water state may itself signal mild water deficit (Jia et al., 2020), whereas the shallow-water response proceeded to end-product accumulation, paralleling submergence-induced reprogramming in arbor willows (Chen et al., 2022). Amino acid–nitrogen and upstream isoprenoid precursors were likewise mobilized ahead of, and progressively consumed during, the rise of terminal defenses (the free C5 isoprenoid precursors themselves were not captured by the widely targeted panel). Whether aromatic carbon finally serves the wall or defense is decided at the branch point downstream of phenylalanine ammonia-lyase (Vogt, 2010; Zhang & Liu, 2015).

p-Coumaroyl-CoA, formed from phenylalanine through PAL, C4H and 4CL, is the branch point shared by the flavonoid and monolignol routes (Fig. 7): CHS/CHI lead into flavonoids, whereas HCT/C3H, CCoAOMT, F5H and CCR/CAD produce H/G/S monolignols (Fraser & Chapple, 2011; Vogt, 2010; Yao et al., 2021; Zhang & Liu, 2015). Under excess-water stress, phenylpropanoid carbon is often held transiently in reversibly esterified or glycosylated forms (Behr et al., 2020; Naoumkina et al., 2010). Indeed, soluble feruloyl conjugates accumulated in adequate water and 6-O-feruloyl-glucose in shallow water, while p-coumaroylquinic acid and sinapyl alcohol were highest in the deep-water control: aromatic carbon was apparently buffered in soluble, reversible conjugates before release for POD/LAC polymerization. The two structural polysaccharides differ in precursor and timing—cellulose is assembled from hexose-derived UDP-Glc (Meents et al., 2018; Polko & Kieber, 2019) and peaked in early adequate water, whereas hemicellulose, built from pentose-phosphate-derived UDP-Xyl/Ara, was deposited last (Crowe et al., 2021; Scheller & Ulvskov, 2010; Zhang et al., 2021; Zhong et al., 2017)—consistent with well-documented stress-driven remodeling of secondary walls (Bonawitz & Chapple, 2010; Le Gall et al., 2015; Moura et al., 2010). Lignin rose to a transient early-shallow-water peak (T3) before returning

to near-control levels; AMP, enriched exactly at T3 and positively correlated with lignin (r = +0.948), reflects the energy and nucleotide demand of that synthesis. Early flavonoid skeletons (chalcones, flavonols, anthocyanins) peaked in adequate water as antioxidants alongside growth (Brunetti et al., 2013; Zhuang et al., 2023), whereas heavily modified polymethoxyflavones and hydrolyzable tannins—sanguiin H4 and ellagic acid at T3, 1,6-di-O-galloylglucose at T4—peaked only in shallow water, where such tannins deter herbivores and pathogens (Niemetz & Gross, 2005); condensed-tannin galloylated flavan-3-ols likewise peaked at T3 (Dixon & Sarnala, 2020), and the *Salix*-characteristic glycosides salicin and Helecin joined the same late window (Boeckler et al., 2011). Because the flavonoid and lignin routes compete for the same p-coumaroyl-CoA flux, shallow-water carbon was preferentially committed to lignin polymerization and terminal defense: cellulose fell 38.8% from its adequate-water peak while RR rose from 0.52 to 0.92, the quantitative signature of the growth–defense trade-off (Herms & Mattson, 1992; Huang et al., 2020; Morrison et al., 2024; Panda et al., 2021).

Weighted gene co-expression network analysis recovered the same structure without supervision (Langfelder & Horvath, 2008): ME5 (103 metabolites), the largest module, correlated most strongly with cellulose (r = +0.94), and its high-loading nodes were the glycolysis, aromatic amino acid, UDP-sugar and early flavonoid metabolites abundant in the adequate-water state—an unsupervised, module-level signature of cellulose-based wall construction. ME9 (12 metabolites) was instead negatively correlated with hemicellulose (r = −0.89); its eigengene was highest in the slender, large-lumen fibers of adequate water and lowest at the late hemicellulose peak, tracking the matrix-polysaccharide phase of secondary-wall thickening. Other module–trait correlations (e.g., ME7 with wall-thickening traits, r = 0.72 to −0.87, p = 0.055–0.17) remain trend-level support interpreted together with pathway-position and chemical-assay evidence. At the metabolite level, vanillic acid methyl ester and γ-Glu-Trp correlated positively with cellulose alongside wall construction, whereas the terminal polymethoxyflavone nobiletin correlated negatively (r = −0.951) and accumulated as cellulose fell, tracing the diversion of structural carbon to terminal defense (Vogt, 2010;

Yobi et al., 2013; Zhuang et al., 2023). Overlaying these correlations on pathway topology (Fig. 7) is more informative than grouping metabolites by chemical class alone (Table S9).

### *4.3 Ecophysiological implications and limitations*

Taken together, the response of *S. suchowensis* to a rising root-zone water content under a shallower groundwater table resolves into a measurable carbon-allocation sequence. In adequate water, carbon flows through glycolysis, the pentose phosphate pathway and the aromatic amino acid gateway into UDP-sugars and early flavonoids; cellulose peaks and fibers are slender, thin-walled and large-lumen with the lowest RR, defining a wall-construction window. In shallow water, lignin rises transiently to thicken the secondary wall and then recedes, after which carbon shifts to the latest, W-shaped hemicellulose peak and to terminal polymethoxyflavones, hydrolyzable tannins, salicinoids and nitrogen-containing or terpenoid defenses, building a coupled physical and chemical defense. The study thus adds a metabolite-level carbon-sink succession (cellulose → lignin → hemicellulose/terminal defense) and a quantitative RR trajectory to the growth–differentiation balance framework under excess soil water (Herms & Mattson, 1992; Morrison et al., 2024). These stages reflect a threshold transition in root-zone water content from deficit through adequacy toward saturation, rather than a depth value per se; this plastic developmental shift likely underpins the tolerance of this riparian species to both drought and periodic waterlogging. Managing the groundwater table is, in effect, managing the developmental and defensive state of the bark.

Several limitations should be noted. First, bark was sampled as bulk periderm and secondary phloem, so the cellular origin of each metabolite—fiber, ray parenchyma, or sieve-element associated—cannot be localized. Second, groundwater table depth co-varies with soil redox potential and nutrient availability, and these co-varying factors could not be fully separated here. Third, free-metabolite abundance allows flux to be inferred only indirectly; enzyme activities and isotopic flux were not measured. Spatial metabolomics, paired transcriptomics and isotope tracing would therefore be needed to test causality.

## 5 Conclusions

Along the root-zone moisture gradient imposed by groundwater table depths of 1.2–0.3 m, *S. suchowensis* phloem fibers underwent a threshold-type, three-stage transition, from a deep-water baseline (RR = 0.65), through an adequate-water wall-construction window (longest, widest fibers; RR 0.52–0.56), to a shallow-water thickening and defense state (RR 0.92). The 419 differentially accumulated metabolites and the WGCNA modules—ME5 tracking the adequate-water cellulose peak and ME9 declining as hemicellulose accumulated last—place this transition on an ordered phenylpropanoid succession, with cellulose, lignin and hemicellulose peaking in strict sequence as carbon moved from structural growth toward a coupled physical–chemical defense. These findings add metabolite-level timing to the growth–differentiation balance framework and identify stage-specific marker metabolites, showing that root-zone water status acts as a physiological switch that directs bark development between structural growth and defense.

## Author Contributions

Hongbing Zheng: Conceptualization, Methodology, Investigation, Formal analysis, Data curation, Writing – original draft, Writing – review and editing, Visualization, Funding acquisition.

## Conflict of Interest

The author declares that they have no known competing financial interests or personal relationships that could have appeared to influence the work reported in this paper.

## Data Availability Statement

The metabolomics data and all other data supporting the findings of this study are included in the article and its Supplementary Materials.

## Acknowledgements of Generative AI Technologies

During the preparation of this work, the author used generative AI-based tools (large language models) to assist with language editing and to improve textual clarity. After using these tools, the author reviewed and edited all content and takes full responsibility for the content of the publication.

## References


Agarwal, P., Fischer, H.D., Camalle, M.D. & Skirycz, A. (2025) Not to be overlooked: dipeptides and their role in plant stress resilience. *Journal of Experimental Botany*, *76*(19), 5738–5747. https://doi.org/10.1093/jxb/eraf311

Baker, P.W., Charlton, A., Johnston, C., Leahy, J.J., Lindegaard, K., Pisano, I., Prendergast, J.P., Preskett, D. & Skinner, C. (2022) A review of willow (Salix spp.) as an integrated biorefinery feedstock. *Industrial Crops and Products*, *189*, 115823. https://doi.org/10.1016/j.indcrop.2022.115823

Behr, M., Neutelings, G., El Jaziri, M. & Baucher, M. (2020) You want it sweeter: how glycosylation affects plant response to oxidative stress. *Frontiers in Plant Science*, *11*, 571399. https://doi.org/10.3389/fpls.2020.571399

Benjamini, Y. & Hochberg, Y. (1995) Controlling the false discovery rate: a practical and powerful approach to multiple testing. *Journal of the Royal Statistical Society: Series B*, *57*(1), 289–300. https://doi.org/10.1111/j.2517-6161.1995.tb02031.x

Boeckler, G.A., Gershenzon, J. & Unsicker, S.B. (2011) Phenolic glycosides of the Salicaceae and their role as anti-herbivore defenses. *Phytochemistry*, *72*(13), 1497–1509. https://doi.org/10.1016/j.phytochem.2011.01.038

Bonawitz, N.D. & Chapple, C. (2010) The genetics of lignin biosynthesis: connecting genotype to phenotype. *Annual Review of Genetics*, *44*, 337–363. https://doi.org/10.1146/annurev-genet-102209-163508

Brunetti, C., Di Ferdinando, M., Fini, A., Pollastri, S. & Tattini, M. (2013) Flavonoids as antioxidants and developmental regulators: relative significance in plants and humans. *International Journal of Molecular Sciences*, *14*(2), 3540–3555. https://doi.org/10.3390/ijms14023540

Bryukhanova, M. & Fonti, P. (2013) Xylem plasticity allows rapid hydraulic adjustment to annual climatic variability. *Trees*, *27*(3), 485–496. https://doi.org/10.1007/s00468-012-0802-8

Chen, L., Liu, L., Yang, G., Li, X., Dai, X., Xue, L. & Yin, T. (2024) Expression quantitative trait locus of wood formation-related genes in Salix suchowensis. *International Journal of Molecular Sciences*, *25*(1), 2247. https://doi.org/10.3390/ijms25010247

Chen, W., Gong, L., Guo, Z., Wang, W., Zhang, H., Liu, X., Yu, S., Xiong, L. & Luo, J. (2013) A

589 novel integrated method for large-scale detection, identification, and quantification of widely
590 targeted metabolites: application in the study of rice metabolomics. *Molecular Plant*, *6*(6),
591 1769–1780. https://doi.org/10.1093/mp/sst080
592 Chen, Y., Yang, J., Guo, H., Du, Y., Liu, G., Yu, C., Zhong, F., Lian, B. & Zhang, J. (2022)
593 Comparative transcriptomic analysis reveals potential mechanisms for high tolerance to
594 submergence in arbor willows. *PeerJ*, *10*, e12881. https://doi.org/10.7717/peerj.12881
595 Crowe, J.D., Hao, P., Pattathil, S., Pan, H., Ding, S.-Y., Hodge, D.B. & Jensen, J.K. (2021) Xylan is
596 critical for proper bundling and alignment of cellulose microfibrils in plant secondary cell walls.
597 *Frontiers in Plant Science*, *12*, 737690. https://doi.org/10.3389/fpls.2021.737690
598 Dai, X., Hu, Q., Cai, Q., Feng, K., Ye, N., Tuskan, G.A., Milne, R., Chen, Y., Wan, Z., Wang, Z.,
599 Luo, W., Wang, K., Wan, D., Wang, M., Wang, J., Liu, J. & Yin, T. (2014) The willow genome
600 and divergent evolution from poplar after the common genome duplication. *Cell Research*,
601 *24*(10), 1274–1277. https://doi.org/10.1038/cr.2014.83
602 Daniel, K. & Hartman, S. (2024) How plant roots respond to waterlogging. *Journal of Experimental*
603 *Botany*, *75*(2), 511–525. https://doi.org/10.1093/jxb/erad332
604 Dixon, R.A. & Sarnala, S. (2020) Proanthocyanidin biosynthesis—a matter of protection. *Plant*
605 *Physiology*, *184*(2), 579–591. https://doi.org/10.1104/pp.20.00973
606 Dominguez, P.G. & Niittylä, T. (2022) Mobile forms of carbon in trees: metabolism and transport.
607 *Tree Physiology*, *42*(3), 458–487. https://doi.org/10.1093/treephys/tpab123
608 Franklin, G.L. (1945) Preparation of thin sections of synthetic resins and wood-resin composites,
609 and a new macerating method. *Nature*, *155*(3924), 51. https://doi.org/10.1038/155051a0
610 Fraser, C.M. & Chapple, C. (2011) The phenylpropanoid pathway in Arabidopsis. *The Arabidopsis*
611 *Book*, *9*, e0152. https://doi.org/10.1199/tab.0152
612 Gui, G., Zhang, Q., Hu, W. & Liu, F. (2024) Application of multiomics analysis to plant flooding
613 response. *Frontiers in Plant Science*, *15*, 1389379. https://doi.org/10.3389/fpls.2024.1389379
614 Herms, D.A. & Mattson, W.J. (1992) The dilemma of plants: to grow or defend. *The Quarterly*
615 *Review of Biology*, *67*(3), 283–335. https://doi.org/10.1086/417659
616 Huang, J., Rücker, A., Schmidt, A., Gleixner, G., Gershenzon, J., Trumbore, S. & Hartmann, H.
617 (2020) Production of constitutive and induced secondary metabolites is coordinated with
618 growth and storage in Norway spruce saplings. *Tree Physiology*, *40*(7), 928–942.

https://doi.org/10.1093/treephys/tpaa040

Jia, H., Wang, L., Li, J., Sun, P., Lu, M. & Hu, J. (2020) Physiological and metabolic responses of Salix sinopurpurea and Salix suchowensis to drought stress. *Trees*, *34*(2), 563–577. https://doi.org/10.1007/s00468-019-01937-z

Kreuzwieser, J. & Rennenberg, H. (2014) Molecular and physiological responses of trees to waterlogging stress. *Plant, Cell & Environment*, *37*(10), 2245–2259. https://doi.org/10.1111/pce.12310

Kuniak, E. & Gajewska, E. (2024) Lipids and lipid-mediated signaling in plant–pathogen interactions. *International Journal of Molecular Sciences*, *25*(13), 7255. https://doi.org/10.3390/ijms25137255

Langfelder, P. & Horvath, S. (2008) WGCNA: an R package for weighted correlation network analysis. *BMC Bioinformatics*, *9*, 559. https://doi.org/10.1186/1471-2105-9-559

Le Gall, H., Philippe, F., Domon, J.-M., Gillet, F., Pelloux, J. & Rayon, C. (2015) Cell wall metabolism in response to abiotic stress. *Plants*, *4*(1), 112–166. https://doi.org/10.3390/plants4010112

Li, C., Xu, M., Cai, X., Han, Z., Si, J. & Chen, D. (2022) Jasmonate signaling pathway modulates plant defense, growth, and their trade-offs. *International Journal of Molecular Sciences*, *23*(7), 3945. https://doi.org/10.3390/ijms23073945

Lim, G.-H., Singhal, R., Kachroo, A. & Kachroo, P. (2017) Fatty acid- and lipid-mediated signaling in plant defense. *Annual Review of Phytopathology*, *55*, 505–536. https://doi.org/10.1146/annurev-phyto-080516-035406

Maeda, H. & Dudareva, N. (2012) The shikimate pathway and aromatic amino acid biosynthesis in plants. *Annual Review of Plant Biology*, *63*, 73–105. https://doi.org/10.1146/annurev-arplant-042811-105439

Meents, M.J., Watanabe, Y. & Samuels, A.L. (2018) The cell biology of secondary cell wall biosynthesis. *Annals of Botany*, *121*(6), 1107–1125. https://doi.org/10.1093/aob/mcy005

Morrison, C.R., Hart, L., Wolf, A.A., Sedio, B.E., Armstrong, W. & Gilbert, L.E. (2024) Growth-chemical defence-metabolomic expression trade-off is relaxed as soil nutrient availability increases for a tropical passion vine. *Functional Ecology*, *38*(5), 1320–1337. https://doi.org/10.1111/1365-2435.14537

649 Moura, J.C.M.S., Bonine, C.A.V., Viana, J.O.F., Dornelas, M.C. & Mazzafera, P. (2010) Abiotic and
650 biotic stresses and changes in the lignin content and structure of plants. *Journal of Integrative*
651 *Plant Biology*, *52*(4), 360–376. https://doi.org/10.1111/j.1744-7909.2010.00892.x
652 Mozo, I., Rodríguez, M.E., Monteoliva, S.I. & Luquez, V.M.C. (2021) Floodwater depth causes
653 different physiological responses during post-flooding in willows. *Frontiers in Plant Science*,
654 *12*, 575090. https://doi.org/10.3389/fpls.2021.575090
655 Naoumkina, M.A., Zhao, Q., Gallego-Giraldo, L., Dai, X., Zhao, P.X. & Dixon, R.A. (2010)
656 Genome-wide analysis of phenylpropanoid defence pathways. *Molecular Plant Pathology*,
657 *11*(6), 829–846. https://doi.org/10.1111/j.1364-3703.2010.00648.x
658 Niemetz, R. & Gross, G.G. (2005) Enzymology of gallotannin and ellagitannin biosynthesis.
659 *Phytochemistry*, *66*(17), 2001–2011. https://doi.org/10.1016/j.phytochem.2005.07.016
660 Obata, T. & Fernie, A.R. (2012) The use of metabolomics to dissect plant responses to abiotic
661 stresses. *Cellular and Molecular Life Sciences*, *69*(19), 3225–3243.
662 https://doi.org/10.1007/s00018-012-1091-5
663 Oktaee, J., Lautenschläger, T., Günther, M., Neinhuis, C., Wagenführ, A., Lindner, M. & Winkler,
664 A. (2017) Characterization of willow bast fibers (Salix spp.) from short-rotation plantation as
665 potential reinforcement for polymer composites. *BioResources*, *12*(2), 4270–4282.
666 https://doi.org/10.15376/biores.12.2.4270-4282
667 Panda, S., Kazachkova, Y. & Aharoni, A. (2021) Catch-22 in specialized metabolism: balancing
668 defense and growth. *Journal of Experimental Botany*, *72*(17), 6027–6041.
669 https://doi.org/10.1093/jxb/erab348
670 Polko, J.K. & Kieber, J.J. (2019) The regulation of cellulose biosynthesis in plants. *The Plant Cell*,
671 *31*(2), 282–296. https://doi.org/10.1105/tpc.18.00760
672 Quiñones Martorello, A.S., Gyenge, J.E., Colabelli, M.N., Petigrosso, L.R. & Fernández, M.E.
673 (2023) Functional responses to multiple sequential abiotic stress (waterlogging-drought) in
674 three woody taxa with different root systems and stress tolerance. *Physiologia Plantarum*,
675 *175*(4), e13958. https://doi.org/10.1111/ppl.13958
676 Rousseeuw, P.J. (1987) Silhouettes: a graphical aid to the interpretation and validation of cluster
677 analysis. *Journal of Computational and Applied Mathematics*, *20*, 53–65.
678 https://doi.org/10.1016/0377-0427(87)90125-7

679 Scheller, H.V. & Ulvskov, P. (2010) Hemicelluloses. *Annual Review of Plant Biology*, *61*, 263–289.
680 https://doi.org/10.1146/annurev-arplant-042809-112315
681 Trygg, J. & Wold, S. (2002) Orthogonal projections to latent structures (O-PLS). *Journal of*
682 *Chemometrics*, *16*(3), 119–128. https://doi.org/10.1002/cem.695
683 Tzin, V. & Galili, G. (2010) New insights into the shikimate and aromatic amino acids biosynthesis
684 pathways in plants. *Molecular Plant*, *3*(6), 956–972. https://doi.org/10.1093/mp/ssq048
685 Vogt, T. (2010) Phenylpropanoid biosynthesis. *Molecular Plant*, *3*(1), 2–20.
686 https://doi.org/10.1093/mp/ssp106
687 Wei, S., Yang, Y. & Yin, T. (2020) The chromosome-scale assembly of the willow genome provides
688 insight into Salicaceae genome evolution. *Horticulture Research*, *7*, 45.
689 https://doi.org/10.1038/s41438-020-0268-6
690 Wei, S., Yang, G., Yang, Y. & Yin, T. (2022) Time-sequential detection of quantitative trait loci and
691 candidate genes underlying the dynamic growth of Salix suchowensis. *Tree Physiology*, *42*(4),
692 877–890. https://doi.org/10.1093/treephys/tpab138
693 Yao, T., Feng, K., Xie, M., Barros, J., Tschaplinski, T.J., Tuskan, G.A., Muchero, W. & Chen, J.G.
694 (2021) Phylogenetic occurrence of the phenylpropanoid pathway and lignin biosynthesis in
695 plants. *Frontiers in Plant Science*, *12*, 704697. https://doi.org/10.3389/fpls.2021.704697
696 Yobi, A., Wone, B.W.M., Xu, W., Alexander, D.C., Guo, L., Ryals, J.A., Oliver, M.J. & Cushman,
697 J.C. (2013) Comparative metabolic profiling between desiccation-sensitive and desiccation-
698 tolerant species of Selaginella reveals insights into the resurrection trait. *The Plant Journal*,
699 *76*(6), 983–999. https://doi.org/10.1111/tpj.12008
700 Zhang, W., Qin, W., Li, H. & Wu, A. (2021) Biosynthesis and transport of nucleotide sugars for
701 plant hemicellulose. *Frontiers in Plant Science*, *12*, 723128.
702 https://doi.org/10.3389/fpls.2021.723128
703 Zhang, X. & Liu, C.-J. (2015) Multifaceted regulations of gateway enzyme phenylalanine ammonia-
704 lyase in the biosynthesis of phenylpropanoids. *Molecular Plant*, *8*(1), 17–27.
705 https://doi.org/10.1016/j.molp.2014.11.001
706 Zhong, R., Cui, D. & Ye, Z.-H. (2017) Cytosol-localized UDP-xylose synthases provide the major
707 source of UDP-xylose for the biosynthesis of xylan and xyloglucan. *Plant and Cell Physiology*,
708 *58*(1), 156–174. https://doi.org/10.1093/pcp/pcw179

709 Zhou, J., Guo, J., Chen, Q., Wang, B., He, X., Zhuge, Q. & Wang, P. (2022) Different color
710 regulation mechanism in willow barks determined using integrated metabolomics and
711 transcriptomics analyses. *BMC Plant Biology*, *22*, 530. https://doi.org/10.1186/s12870-022-
712 03909-x
713 Zhuang, W., Li, Y., Shu, X., Pu, Y., Wang, X., Wang, T. & Wang, Z. (2023) The classification,
714 molecular structure and biological biosynthesis of flavonoids, and their roles in biotic and
715 abiotic stresses. *Molecules*, *28*(8), 3599. https://doi.org/10.3390/molecules28083599

**Supporting Information**

The following supporting information is available as part of the online article:

**Table S1.** Descriptive statistics of the four growth traits (plant height and basal, middle and tip diameters), with plot-level replication.

**Table S2.** Treatment means, standard errors and within-row z-scores of the 14 integrated phenotypes.

**Table S3.** Descriptive statistics of the seven bark-fiber morphological traits, including valid measured counts (about 90 fibers per treatment) and fold change versus CK.

**Table S4.** Cellulose, hemicellulose and lignin contents (n = 4), with means, SD/SE and percentage change versus CK.

**Table S5.** KEGG hypergeometric enrichment (381-metabolite universe, Benjamini–Hochberg correction; P and FDR shown) for the overall 419 DAMs and ten pairwise comparisons.

**Table S6.** Master table of the 419 DAMs: treatment means, SE, within-row z-scores and K-means (K = 8) cluster assignment.

**Table S7.** Numbers of up- and down-regulated DAMs and chemical-class composition for ten pairwise comparisons.

**Table S8.** Raw quantitative peak areas of the 419 DAMs across the 15 samples (five treatments × three replicates).

**Table S9.** Significant metabolite–trait correlation pairs ($|r| > 0.85$, $p < 0.05$), with core-robust and Fig. 6B pairs flagged.

**Table S10.** Full correlation matrices: metabolite × trait Pearson r and p values (S10-1 to S10-3) and module eigengene × phenotype r and p values (S10-4 and S10-5).

**Table S11.** OPLS-DA model fit and 200-permutation validation for ten pairwise comparisons.

**Table S12.** Full table of the 1,351 annotated metabolite peaks detected by UPLC-ESI-MS/MS, reporting for each metabolite the metabolite name, chemical class, Q1 (precursor) and Q3 (product) m/z, ion mode, molecular formula, CAS and KEGG identifiers (MWDB V1.0); retention time, declustering potential, collision energy and the basis of identification (authentic-standard validation or in-house spectral-library

and retention-time matching) are additionally provided for 30 representative metabolites spanning the pathways analysed.

## Figure legends

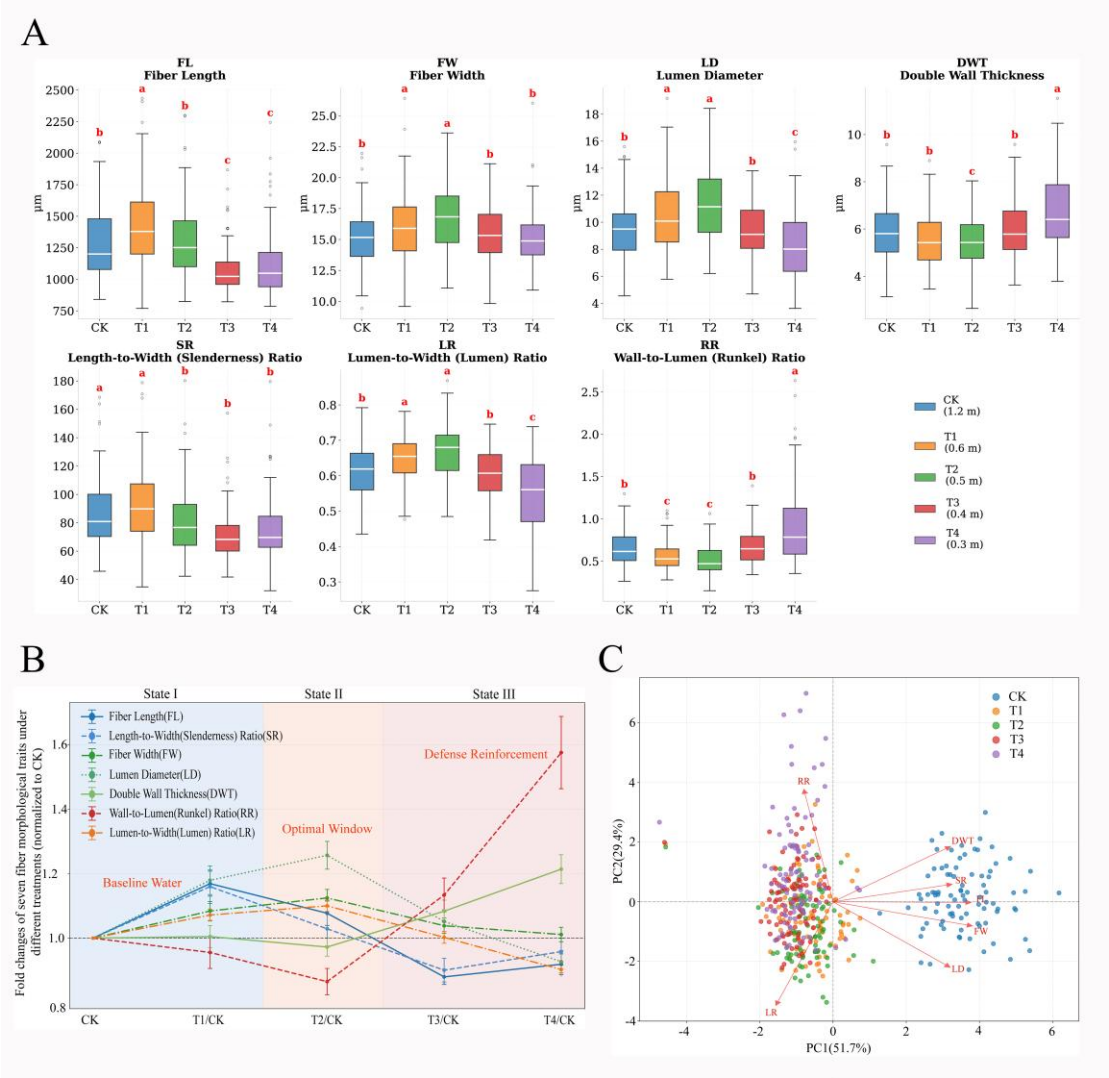


**Figure 1.** Three-stage responses of bark (phloem/bast) fiber morphology of *Salix suchowensis* along the groundwater-table gradient.

(A) Means ± standard errors of seven fiber morphological traits (FL, fiber length; FW, fiber width; LD, lumen diameter; DWT, double-wall thickness; SR, length-to-width ratio; LR, lumen-to-width ratio; RR, wall-to-lumen ratio) across CK–T4 (approximately 90 intact fibers per treatment, with about 22–23 fibers from each of the four plots). (B) Fold changes of each trait relative to CK. (C) Principal component analysis (PCA) biplot of fiber morphology; the first two principal components together explained 81.1% of the variance, with CK, T1/T2, and T3/T4 separated sequentially along PC1.

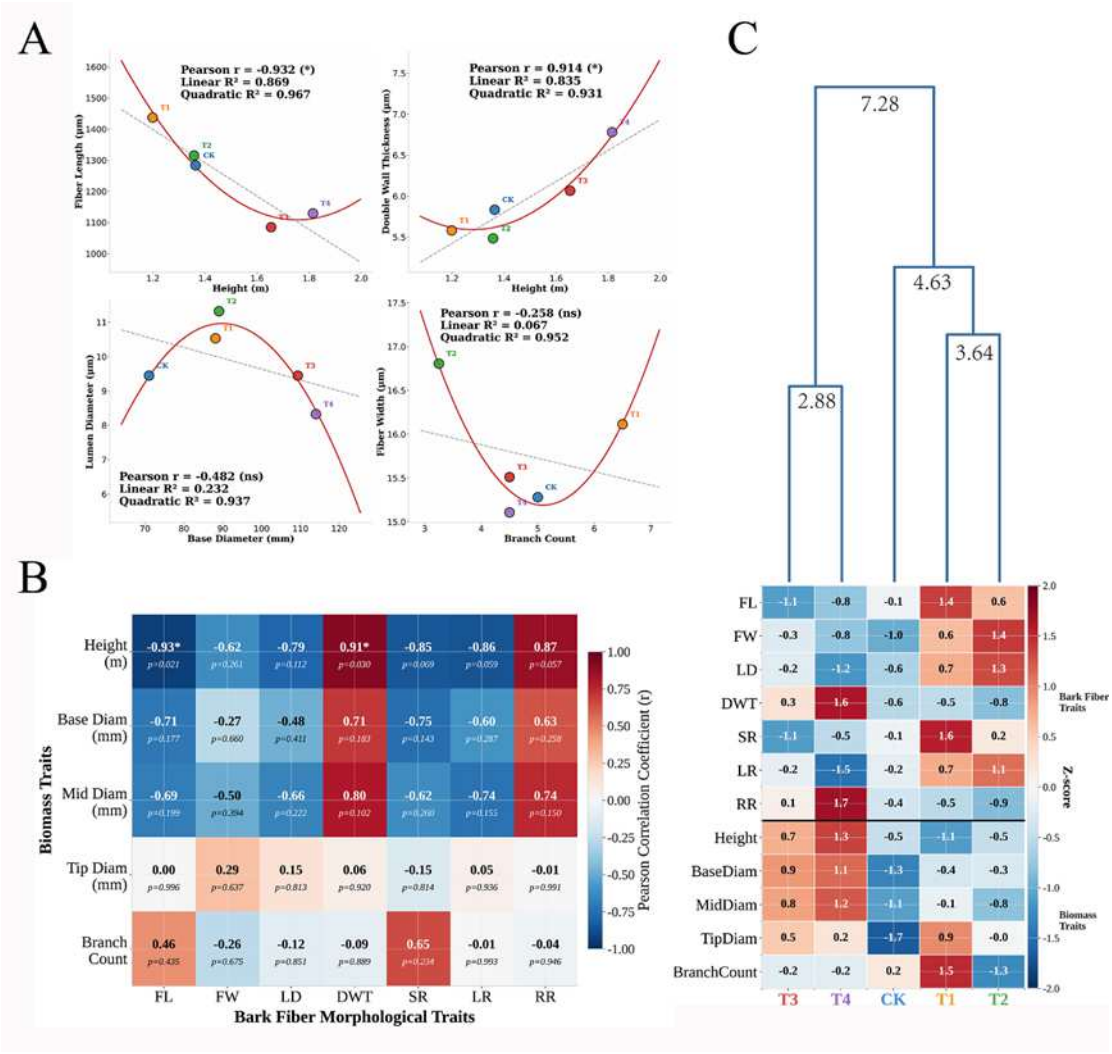


**Figure 2.** Non-linear coordination between growth traits and fiber morphology. (A) Linear and quadratic polynomial regressions of plant height and basal diameter against fiber traits (both model types are shown with coefficients of determination; plant height–FL quadratic $R^2 = 0.967$; plant height–DWT $R^2 = 0.931$; basal diameter–LD $R^2 = 0.937$). (B) Correlation heatmap of 14 integrated phenotypes (Pearson for approximately normal variables and Spearman otherwise; color denotes r; × marks $p \geq 0.05$). (C) Bidirectional hierarchical clustering (Euclidean distance, Ward's method) of five treatments and seven fiber traits based on standardized values.

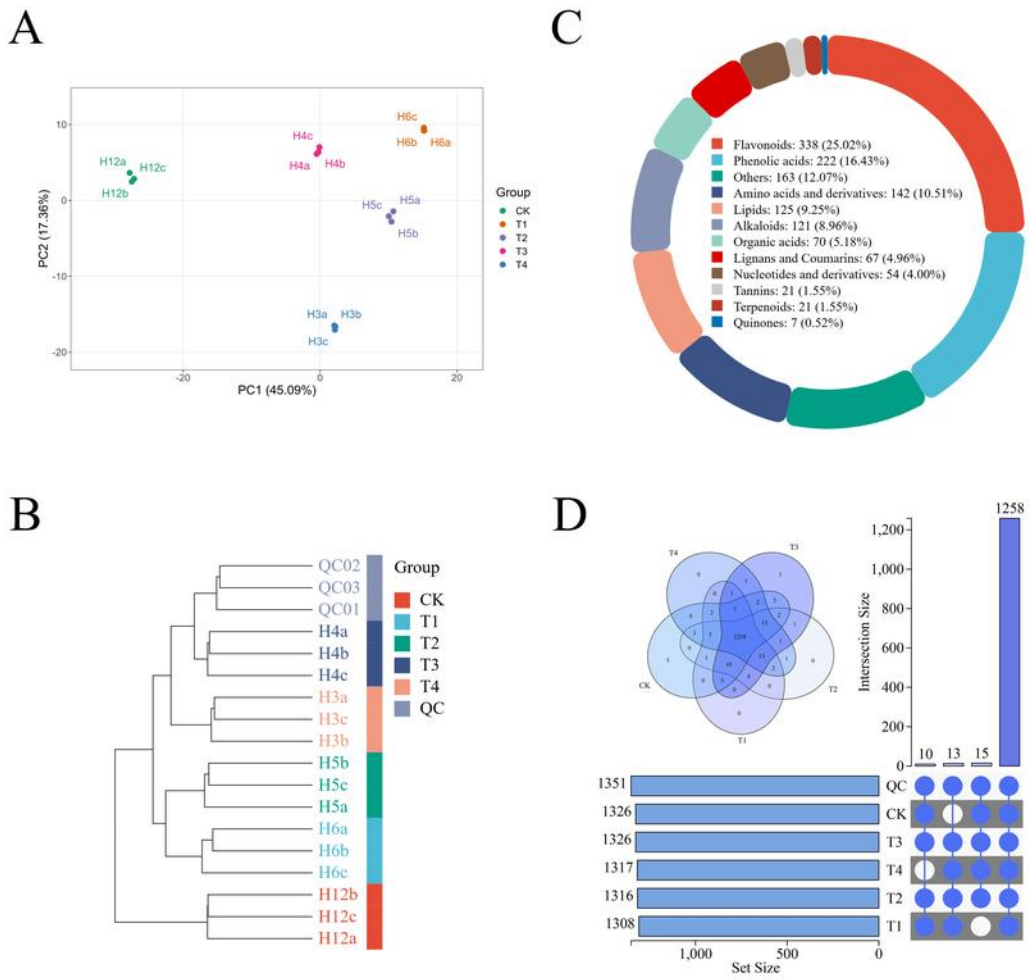


771

772 **Figure 3.** Global metabolomic architecture supporting the three-stage model.

773 (A) PCA score plot of the 1,351 detected metabolites after excluding QC samples (PC1

774 = 45.09%, PC2 = 17.36%). (B) Hierarchical clustering of samples. (C) MWDB Class I

775 chemical class composition (338 flavonoids, 25.02%; 222 phenolic acids, 16.43%). (D)

776 Venn and UpSet analyses of metabolite detection across the five treatments (1,258

777 metabolites (93.12%) were detected in all five; the remaining 93 were detected in four

778 (50), three (23), or two (14) treatments, with only six confined to a single treatment

779 (five in CK and one in T3), indicating a >93% conserved metabolic core and

780 predominantly quantitative rather than treatment-specific differences).

781

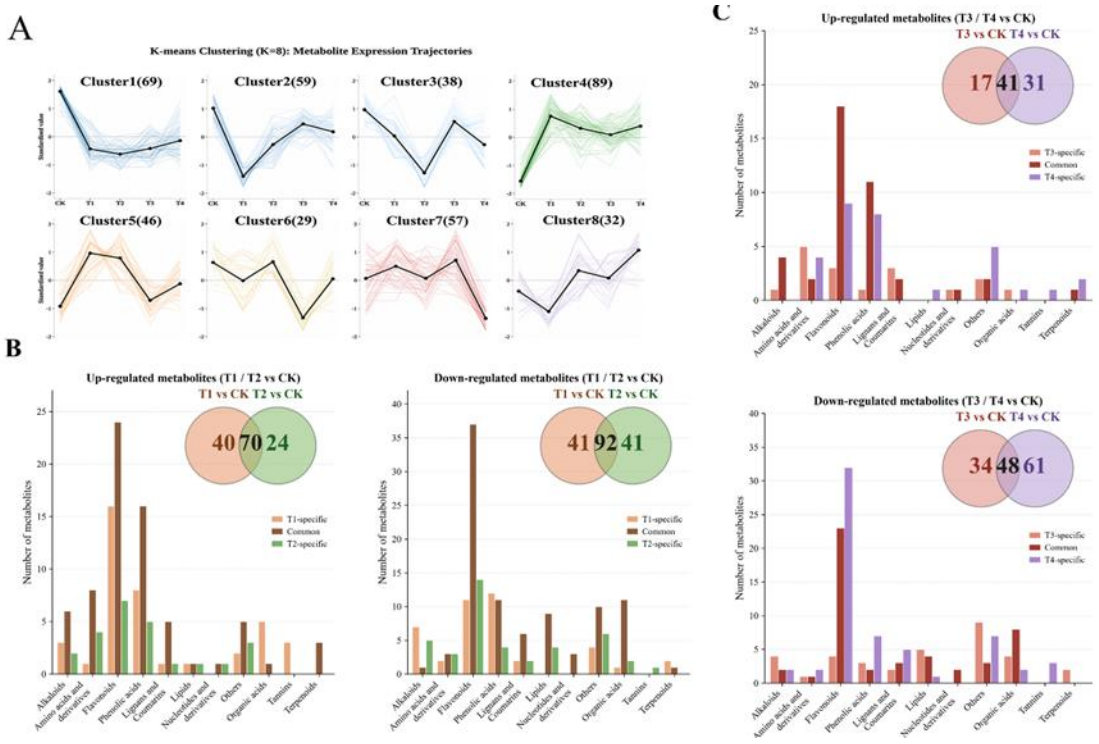


**Figure 4.** K-means temporal trajectories (K = 8) and stage-wise up/down-regulation classification of the 419 differentially accumulated metabolites (DAMs).

(A) K-means clustering (K = 8) partitioned the 419 DAMs into eight clusters (n = 69, 59, 38, 89, 46, 29, 57, and 32, respectively). The vertical axis represents row-standardized values of the log10 means across the five treatments; thin lines denote individual metabolites, and thick lines denote cluster means. Based on peak positions, the clusters were grouped into a CK baseline type (Clusters 1/2/3, 166 metabolites), a CK/T2 double-high type (Cluster 6, 29 metabolites), a T1 peak type (Clusters 4/5, 135 metabolites), a T3 peak type (Cluster 7, 57 metabolites), and a T4 peak type (Cluster 8, 32 metabolites), corresponding to the three stages State I/II/III. (B) Bar charts and Venn diagrams showing the MWDB chemical classes of up- and down-regulated metabolites for T1 vs CK and T2 vs CK (up-regulated: 40 T1-specific, 70 shared, 24 T2-specific; down-regulated: 41 T1-specific, 92 shared, 41 T2-specific). (C) Bar charts and Venn diagrams showing the up- and down-regulated classes for T3 vs CK and T4 vs CK (up-regulated: 17 T3-specific, 41 shared, 31 T4-specific; down-regulated: 34 T3-specific, 48 shared, 61 T4-specific); bar height indicates the number of metabolites in each class.

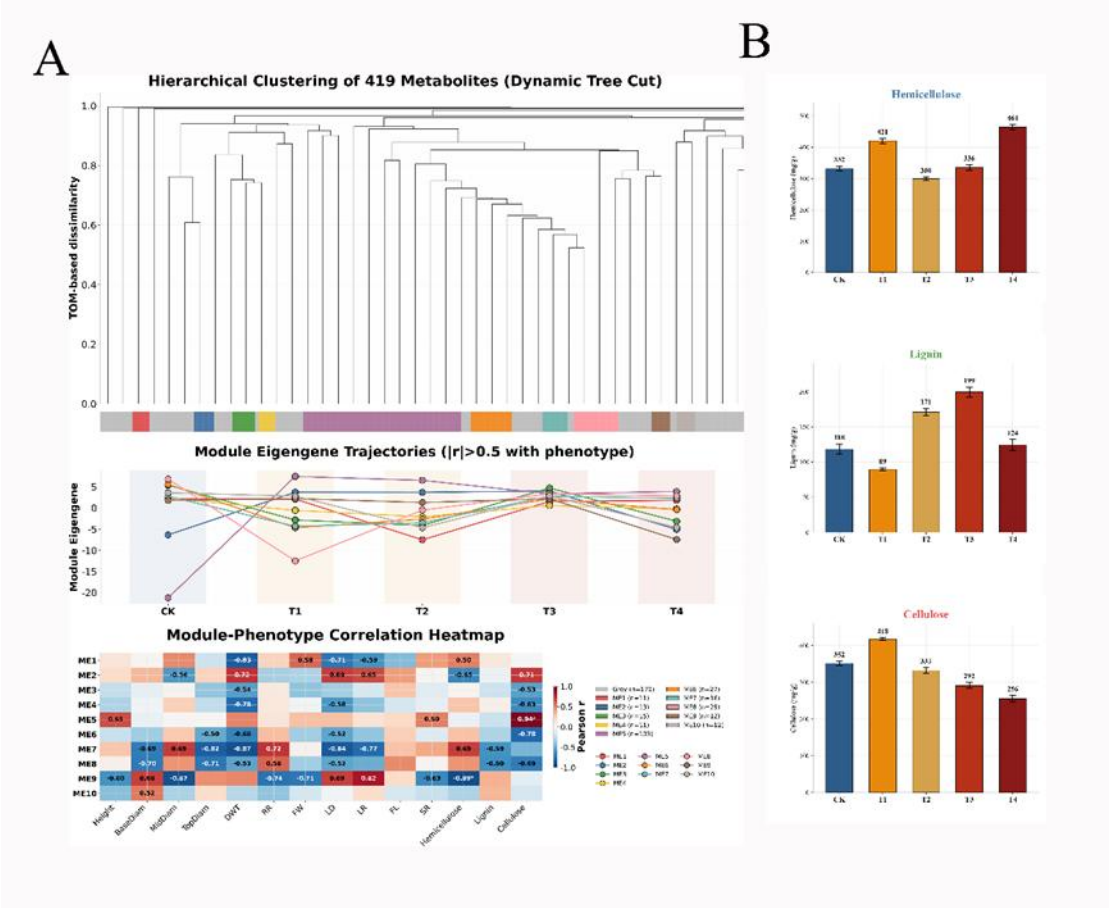


**Figure 5.** WGCNA module–trait network and dynamics of the three major cell-wall components.

(A) Pearson correlation heatmap between module eigengenes of the 10 co-expression modules (ME1–ME10) and the 14 phenotypes, computed across five treatment means (n = 5; values in cells are correlation coefficients r; *p < 0.05 (no pair reached p < 0.01); ME5 (103 metabolites) is most strongly correlated with cellulose (r = +0.94) and ME9 (12 metabolites) is negatively correlated with hemicellulose (r = −0.89), the only two significant module–trait pairs; numeric r and two-sided p values are tabulated in Table S10 (S10-4 and S10-5). (B) Trajectories of cellulose, hemicellulose, and lignin contents (mg g−1) along CK–T4 (means ± standard errors); the three components peaked at T1, T4, and T3, respectively, with strictly staggered peak times.

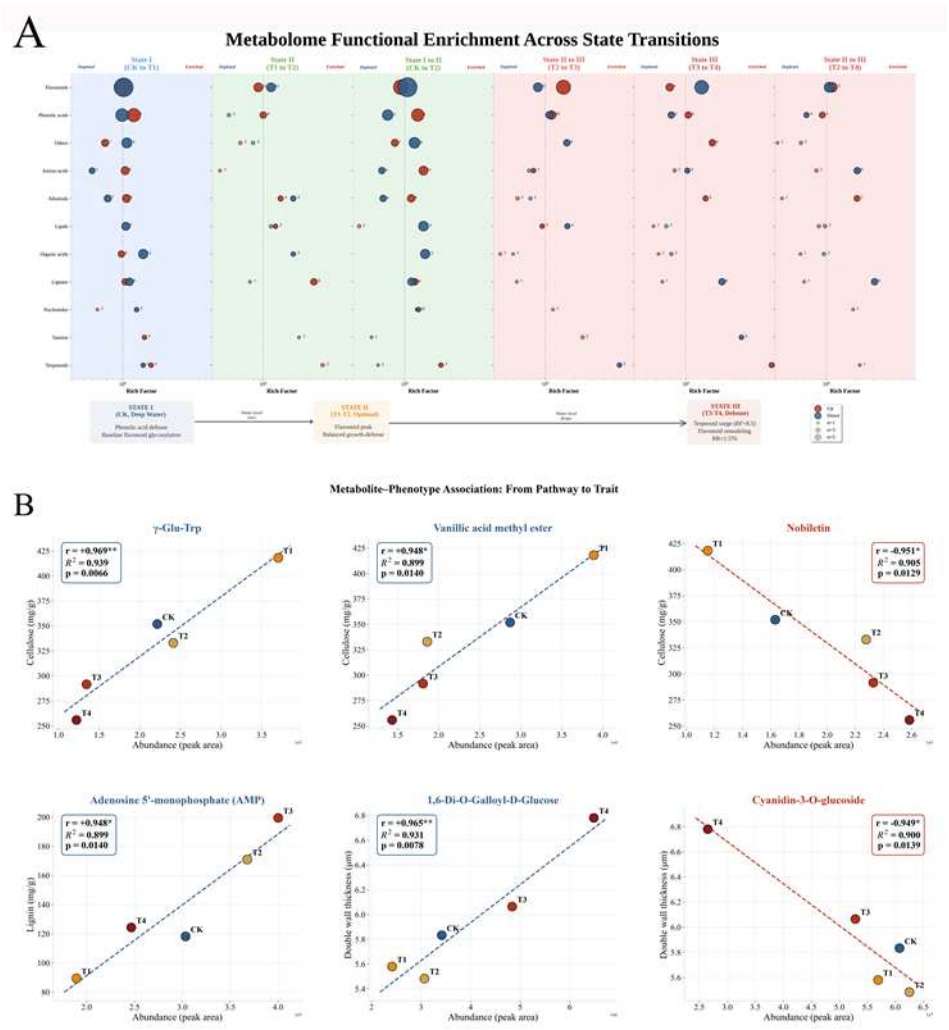


**Figure 6.** Class-level functional enrichment of differentially accumulated metabolites (DAMs) across state transitions and metabolite–trait associations for six core metabolites.

(A) To encompass both adjacent state transitions and cross-stage anchors, six representative comparisons (CK→T1, T1→T2, CK→T2, T2→T3, T3→T4, and T2→T4) were selected to generate bubble plots showing the enrichment/depletion of each chemical class (vertical axis, classified according to MWDB Class I). Red indicates enrichment of that class in the corresponding transition (up-regulation predominates), and blue indicates depletion (down-regulation predominates). The horizontal axis represents the Rich factor (log scale), with depletion to the left and enrichment to the right of the central dashed line. Bubble size and the number inside indicate n, the number of differentially accumulated metabolites hit in that class. Panel background colors and the bottom timeline correspond to the three stages: State I (deep-

water), State II (adequate-water), and State III (shallow-water defense). (B) Scatter correlations of six core metabolites (γ-Glu-Trp, vanillic acid methyl ester, nobiletin, 1,6-di-O-galloylglucose, cyanidin-3-O-glucoside, and adenosine 5′-monophosphate [AMP]) with cellulose, double-wall thickness (DWT), or lignin (including fitted lines, with Pearson r, coefficient of determination $R^2$, and p values; *p < 0.05, **p < 0.01; all satisfy |r| > 0.85). Results of KEGG pathway-level enrichment tests are presented in Section 3.3 and Table S5.

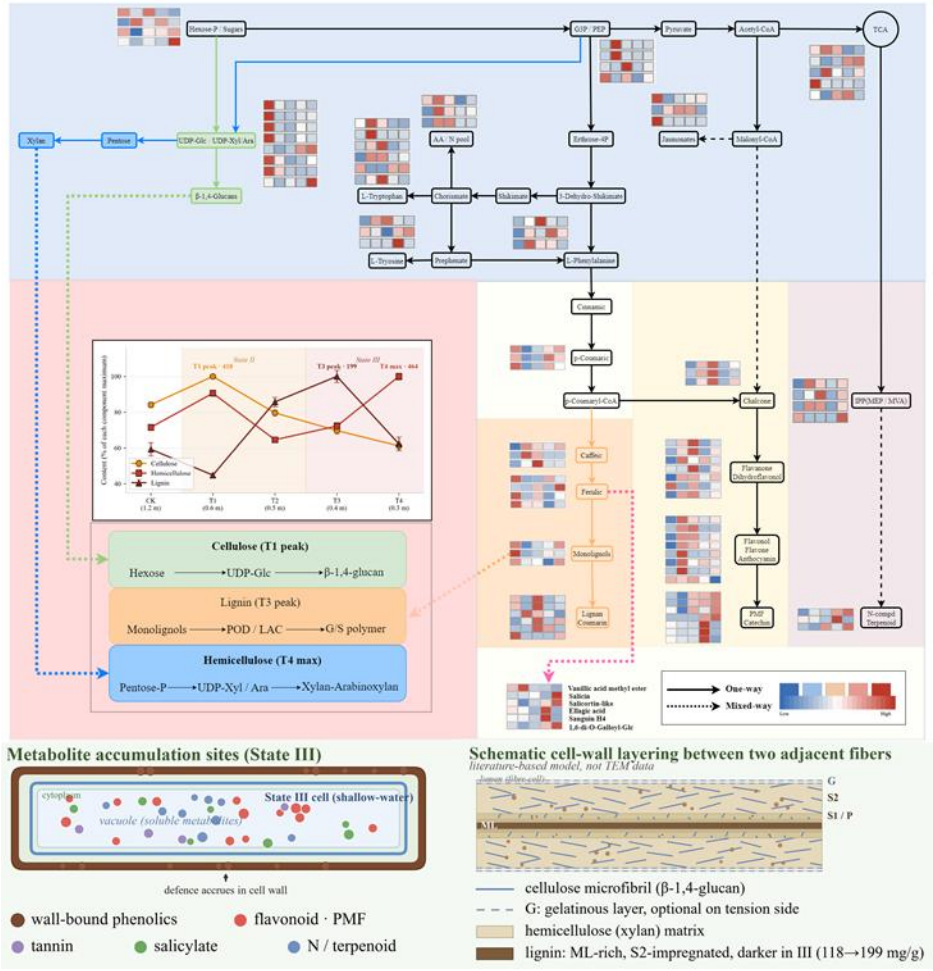


**Figure 7.** Integrated map of metabolic reprogramming and the associated fiber-cell-wall phenotypes in *Salix suchowensis* bark along the groundwater-table gradient (CK→T4).

The main pathway region highlights 89 nodes assignable to central carbon metabolism, the shikimate–aromatic amino acid pathway, phenylpropanoid metabolism, and cell-wall biosynthesis. Heatmaps beside the nodes show row-wise z-scores of the mean

values of three replicates across the five treatments (red, high; blue, low), and the section colors correspond to the three stages. The bottom panel shows, from left to right: longitudinal fiber morphology; a literature-based schematic of the adjacent fiber wall layer structure (ML, middle lamella; P, primary wall; S1/S2, secondary wall layers; G, gelatinous layer visible on the tension side of some phloem fibers; this cross-section is a literature-based schematic); and the trajectories of the three major wall components (determined by independent chemical assays, distinct from the free metabolite heatmaps) across treatments, together with the metabolite accumulation sites in State III. State I = CK; II = T1/T2 (adequate-water growth and wall construction); III = T3/T4 (physical–chemical defense).

## Supplementary Files

This is a list of supplementary files associated with this preprint. Click to download.

- SupplementaryTablesS1S12.xlsx